TU Delft

Delft University of Technology

Nanoengineering of Crystal and Amorphous Surfaces of Pharmaceutical Particles for Biomedical Applications

Zhang, Di; La Zara, Damiano; Quayle, Michael J.; Petersson, Gunilla; Van Ommen, J. Ruud; Folestad, Staffan

DOI
10.1021/acsabm.8b00805

Publication date
2019

Document Version
Accepted author manuscript

Published in
ACS Applied Nano Materials

Citation (APA)
Zhang, D., La Zara, D., Quayle, M. J., Petersson, G., Van Ommen, J. R., & Folestad, S. (2019). Nanoengineering of Crystal and Amorphous Surfaces of Pharmaceutical Particles for Biomedical Applications. *ACS Applied Nano Materials*, *2*(4), 1518-1530. https://doi.org/10.1021/acsabm.8b00805

Important note
To cite this publication, please use the final published version (if applicable).
Please check the document version above.

Copyright
Other than for strictly personal use, it is not permitted to download, forward or distribute the text or part of it, without the consent of the author(s) and/or copyright holder(s), unless the work is under an open content license such as Creative Commons.

Takedown policy
Please contact us and provide details if you believe this document breaches copyrights.
We will remove access to the work immediately and investigate your claim.

This work is downloaded from Delft University of Technology.
For technical reasons the number of authors shown on this cover page is limited to a maximum of 10.

ACS APPLIED BIO MATERIALS

TU Delft

Subscriber access provided by Delft University of Technology

Article

Nano-engineering of crystal and amorphous surfaces of pharmaceutical particles for biomedical applications

Di Zhang, Damiano La Zara, Michael J. Quayle, gunilla petersson, J. Ruud van Ommen, and Staffan Folestad

ACS Appl. Bio Mater., **Just Accepted Manuscript** • DOI: 10.1021/acsabm.8b00805 • Publication Date (Web): 01 Mar 2019

Downloaded from http://pubs.acs.org on March 4, 2019

Just Accepted

"Just Accepted" manuscripts have been peer-reviewed and accepted for publication. They are posted online prior to technical editing, formatting for publication and author proofing. The American Chemical Society provides "Just Accepted" as a service to the research community to expedite the dissemination of scientific material as soon as possible after acceptance. "Just Accepted" manuscripts appear in full in PDF format accompanied by an HTML abstract. "Just Accepted" manuscripts have been fully peer reviewed, but should not be considered the official version of record. They are citable by the Digital Object Identifier (DOI®). "Just Accepted" is an optional service offered to authors. Therefore, the "Just Accepted" Web site may not include all articles that will be published in the journal. After a manuscript is technically edited and formatted, it will be removed from the "Just Accepted" Web site and published as an ASAP article. Note that technical editing may introduce minor changes to the manuscript text and/or graphics which could affect content, and all legal disclaimers and ethical guidelines that apply to the journal pertain. ACS cannot be held responsible for errors or consequences arising from the use of information contained in these "Just Accepted" manuscripts.

ACS Publications

is published by the American Chemical Society. 1155 Sixteenth Street N.W., Washington, DC 20036

Published by American Chemical Society. Copyright © American Chemical Society. However, no copyright claim is made to original U.S. Government works, or works produced by employees of any Commonwealth realm Crown government in the course of their duties.

Nano-engineering of crystal and amorphous surfaces of pharmaceutical particles for biomedical applications

Di Zhang,[a, ξ] Damiano La Zara[b,ξ], Michael J. Quayle,[a] Gunilla Petersson,[a] J. Ruud van Ommen,[b] and Staffan Folestad [a,†]

[a]AstraZeneca R&D Gothenburg, Pepparedsleden 1, Mölndal, SE-431 83, Sweden.

[b]Department of Chemical Engineering, Delft University of Technology, Van der Maasweg 9, 2629 HZ Delft, the Netherlands.

[ξ] These authors contributed equally to this work.

†Corresponding author: Email: staffan.folestad@astrazeneca.com.

KEYWORDS: atomic layer deposition, surface modification, alumina, lactose, pharmaceutical, powders, slowed dissolution, improved dispersibility

ABSTRACT

The morphology, size and surface properties of pharmaceutical particles form an essential role in the therapeutic performance of active pharmaceutical ingredients (APIs) and excipients as constituents in various drug delivery systems and clinical applications. Recent advances in methods for surface modification, however, rely heavily on liquid-phase based modification processes and afford limited control over the thickness and conformality of the coating. Atomic layer deposition (ALD), on the other hand, enables the formation of conformal nanoscale films on complex structures with thickness control on the molecular level, whilst maintaining the substrate particle size and morphology. Moreover, this enables nanoengineering of surfaces of pharmaceutical particles also in the dry state.

Successful nano-engineeering of crystal and amorphous surfaces of pharmaceutical particles is demonstrated in this study whereby functional properties, such as dissolution and dispersability, were tailored for drug delivery applications. This expands on our initial work on ALD of alumina on pharmaceutical particles within the lower micro- to higher nano-size ranges to here probe both crystalline and amorphous lactose substrate surfaces (d_{50} 3.5 and 21 um). In addition, both water and ozone co-reactants were evaluated; the latter having not been evaluated previously for pharmaceutical particles.

The deposition process is carried out at ambient conditions in a fluidized bed reactor for a low number of cycles (i.e. from 4 to14).

Improved dissolution and extended release were achieved by the ALD nanoengineering of both crystalline and amorphous surfaces. This novel concept opens up exciting opportunities to produce more complex materials and structures using temperature and moisture sensitive drugs, e.g. targeting and drug delivery opportunities, as well as delivering new functionalities for novel applications in the pharmaceutical, medical, biological, and advanced materials fields. The prospects for advancing inhaled drug delivery are exemplified by the ALD surface nano-engineering concept.

1. INTRODUCTION

Active Pharmaceutical Ingredients (APIs) and pharmaceutical excipients are most often small-molecule organic solid particulate materials present in the form of powders, granules, etc. Such particles are usually irregularly shaped with surfaces of high rugosity, and along with particle size play an important role in pharmaceutical and clinical applications. Pharmaceutical powders are often cohesive and may lead to processing problems during manufacturing, such as agglomeration and poor flow or segregation. The surface chemistry of pharmaceutical particles also has a strong influence on their dissolution behavior in formulated products.[1] Many pharmaceutical particles are sensitive to temperature and humidity. Often the amorphous phase may be induced during processing, particularly at surfaces, e.g. micronisation, and may lead to charged material. The amorphous phase is a high-energy state which is unstable with respect to the crystalline form, thus making the amorphous pharmaceutical materials sensitive to humidity. The stabilization of solid state forms (e.g. amorphous, metastable polymorphs, hydrates) during pharmaceutical manufacture and shelf-life brings additional challenges. There is, therefore, an unmet need for technological solutions to provide surface modification of pharmaceutical powders that leads to

functional improvements at both the single particle and powder levels. Additional challenges such as dispersability of powders are common within drug development, for example, inhaled drug delivery.

Current approaches for coating pharmaceutical particles have limited control over the thickness and conformality of the coating and do not provide control at the atomic or molecular scale. On the other hand, Atomic Layer Deposition (ALD) has been widely used for functional pin-hole free thin film deposition on inorganic substrates with applications in solar cells, semi-conductors,[2-3] ceramics, and medical devices.[4] Reported studies of ALD on particulate organic substrates have been limited to a few studies based on polymeric materials,[5-6] and only very recently we,[7] and others,[8-10] have published on pharmaceutical materials. In our recent work, we have demonstrated that alumina thin films at atomic scale can be deposited on pharmaceutical particles via ALD using TMA and water precursors under near ambient conditions using an assisted fluidised bed reactor.[7] As few as 2 - 14 coating cycles successfully altered particle properties such as dispersibility and dissolution. The deposition of alumina film on budesonide could be precisely controlled and was very close to an ideal ALD process. ALD of metal oxides on minitablets[9] and acetaminophen primary particles[8] in the size range of tens to hundreds of microns have been reported by Kääriäinen et al. The studies showed that ALD permits a simple and rapid method for the ultrathin coating (nanolayering) of minitablets, and provided nanoscale range TiO_2 coatings on porous minitablets.[9] The ALD-surface-modified acetaminophen particles with Al_2O_3, TiO_2 and ZnO thin film did not undergo degradation during the ALD coating process and maintained the stable polymorphic crystalline form. The coated acetaminophen particles showed slowed drug release.[8] Hellrup et al. have developed dense metal oxide nanoshells on particles of spray-dried amorphous lactose via ALD.[10] The deposition process did not induce recrystallization of the amorphous lactose, and the so-called nanoshells (5 sets of 50 cycles) inhibited moisture sorption during the storage at 75% RH for 6 months and therefore effectively protected the amorphous structures from recrystallization.[10] In these

related works ALD cycles of 20-500 were used and water vapour was applied as a co-reactant with operating temperatures above 50°C.

The biocomptability of aluminium and alumina (Al_2O_3) is well studied and summarized in references 7 and 8. The data are encouraging for the use of alumina thin film coated pharmaceutical particles for clinical applications. Al_2O_3 is one of the widely studied materials grown by ALD to improve oxygen and moisture barrier properties of synthetic and biobased plastics, biopolymers, and fiber-based materials, therefore, with great potential for controlling drug dissolution rates[11].

ALD of alumina thin films using trimethylaluminum (TMA) and water under ambient conditions has been extensively reported for other applications due to the ease of the process: the reaction of the highly reactive precursor trimethylaluminum [$Al(CH_3)_3$] (TMA) and water vapor runs easily, even under ambient conditions.[12-13] The deposition mechanism is shown in Equation 1 below:[14]

$$2Al(CH_3)_3 + 3H_2O \longrightarrow Al_2O_3 + 6CH_4 \qquad \textit{Equation 1}$$

One drawback is, however, that the OH radical acts as an impurity at the interface and may degrade the quality of the alumina films.[15] In addition, water can adsorb on reactor walls and is difficult to purge.[16] These disadvantages are more pronounced when operating at room temperature.

The use of ozone (O_3) as an oxygen source in metal-oxide ALD has been studied to overcome the limitations in TMA/H_2O ALD. The following reaction takes place (Equation 2):[17]

$$2Al(CH_3)_3 + O_3 \longrightarrow Al_2O_3 + 3C_2H_6 \qquad \textit{Equation 2}$$

The high electrochemical potential of ozone, high volatility and shortening purge times between cycles offer fast reaction rates and significant advantages throughout the ALD process.[18] The absence of hydrogen in the ozone molecule results in a reduced risk of hydrogen and hydroxyl contamination in the growing film. Compared to TMA/H_2O, alumina films deposited using TMA/O_3 have been shown to

result in an improved surface morphology and superior quality for micro-electric devices,[19] and less defects (such as Al-Al and OH bonds) demonstrating improved interface characteristics.[15] Greatly improved film uniformity/coverage and deposition rate has been indicated with the TMA/O_3 because of accelerated TMA nucleation.[20]

In the recent papers on coating pharmaceutical substrates using ALD,[7-10] water is the only oxidant demonstrated. For hygroscopic materials and those with poor processability, using water under ambient conditions carries the risks of inducing degraded film quality and poor process control. The aim of the present study was therefore to extend the successful coating of pharmaceutical particles by ALD to also include evaluation of co-reactants for ALD. This study comprises the film deposition process contrasting TMA/ozone to TMA/water for micronized lactose particles with two sizes (d_{50} 3.5 and 21μm) and surface structure (crystalline and amorphous) at ambient conditions together with advanced particle characterisation. Lactose is a simple sugar found in milk and is widely used in the pharmaceutical industry.[21] The most well-known crystalline forms are α- and β-lactose. Lactose can also be readily produced in the amorphous form. Herein, lactose is used as a model material since it exhibits properties commonly seen in pharmaceutical materials, e.g. polymorphism, hydration and readily available amorphous forms.

The objectives of this work are to explore:

1) potential advantages of ozone as an oxidant compared to water for ALD processing and engineering high quality conformal coatings of pharmaceutical particles;

2) the effect of particle size and the impact of particle surfaces (crystalline vs. amorphous) on ALD processing, quality of coatings, and any differences oxidants have.

Evaluation of the coatings and single particle and bulk property functional testing is carried out using tools developed in our earlier work.[7] In addition, solid state changes during ALD processing were probed using thermal chemistry and advanced solid-state characterisation.

2. MATERIALS AND METHODS

2.1. Materials

Semiconductor grade trimethylaluminum (TMA) was purchased from Akzo Nobel HPMO (Amersfoort, The Netherlands) in a 600 mL stainless steel bubbler (WW-600). Milled α-lactose monohydrate particles Lactohale® 201 (L20µm) (d_{50} 21 µm) and Lactohale® 300 (L3µm) (d_{50} 3.5 µm) were donated by DFE pharma (Germany). The as-received particles were used as reference (Ref) samples. The specific surface area (SSA) of the particles was measured by Brunauer-Emmett-Teller (BET) N_2-sorption surface area analyzer (Micromeritics TriStar 3000 or TriStar 3020, United States). About 1 – 1.5 g particles were used for the BET surface area measurements. Prior to the measurement the particles were degassed for at least 3 hours at 25 °C using SmartPrep or VacPrep (Micromeritics, United States). For each sample 2-4 parallel tests were carried out.

To study the changes in the structures of the samples during the ALD process, dehydrated samples of the reference particles were prepared either by thermal gravimetric analysis (TGA) or by heating around 5 g of powder on an aluminium foil in an oven either in air or under vacuum conditions. The details of the dehydration conditions and the measured BET surface are listed in **Table 1**. The degree of dehydration was calculated based on the measured weight before and after the dehydration, assuming water removed by TGA was originating from the structure of α-lactose monohydrate (initial sample).

Table 1. Dehydration treatment of the lactose Ref. samples at different conditions.

Sample	Dehydration conditions	Dehydration degree	BET SSA (m^2/g)
L20µm 25% dh	under vacuum at 60°C for 27h	25%	0.98

L3µm 76% dh	under vacuum at 60°C for 23h	76%	4.94
L3µm 97% dh	In air at 120°C for 20min	97%	-
L3µm 47.5% dh	by TGA at 80°C for 20min	47.5%	
L3µm 100% dh	by TGA at 110°C for 20min	100%	

2.2. Fluidised Bed ALD Processing of lactose particles

Fluidization is one of the most effective techniques available to disperse micro- and nano-meter sized particles.[221] It has been used in ALD processes to ensure a good dispersion of particles.[232] However, fine particles tend to form agglomerates during the fluidization due to the large cohesive forces exhibited by organic fine particles.[221] On the one hand, this is desired since it prevents the blow-out of fine particles. On the other hand, too severe agglomeration will lead to poor mixing. For cohesive powders, it is often necessary to apply an assisting method, such as vibration,[243] to obtain proper fluidization. A general description is included here. Al_2O_3 films were deposited in a purpose-built fluidized bed reactor consisting of a glass column of 26 mm in diameter and 500 mm in length, placed on a single motor Paja PTL 40/40-24 vertical vibration table to assist the fluidization. The vibration table was operated at 35 Hz, and provides a vibration amplitude of 2 mm to the column. An infrared lamp placed parallel to the column, and a type-K thermocouple inserted in the column, were used to control and measure the bed temperature. Two stainless-steel distributor plates with pore size of 37 µm, placed at the bottom and top of the column, are used to obtain a homogeneous distribution of the gas inside the column and to prevent particles from leaving the reactor. TMA was kept in a stainless-steel bubbler at 30 °C during the coating experiments. The co-reactant, either demineralized water or ozone, generated by a Certizon Ozonizer (C200, Erwin Sander Elektroapparatebau GmbH, Germany) with an output of 200 mg O_3/h, was kept at room temperature (i.e., ~20 °C). Pressurized nitrogen (grade 5.0) was provided to the column as the carrier gas. The column was always kept at atmospheric pressure. During the start-up of each experiment, nitrogen was first used to drive away the air. The off-gas of the fluidized bed was led through a series of washing bubblers filled with Kaydol oil to remove possible traces of unreacted co-reactants and reaction

by-products. The precursor bubblers, the fluidized bed reactor and the washing bubblers were placed inside a nitrogen-blanketing cabinet as a TMA safety measure. The cabinet was operated at an O_2 concentration below 6%.

Table 2. Experimental parameters of the ALD process.

Sample	Weight (g)	Flow rate (L/min)	Process temp. (°C)	BET SSA (m^2/g)	Calculated dosing time (s)		Experimental dosing time (s) TMA–N_2–H_2O/O_3–N_2	Cycles
					TMA	H_2O/O_3		
L20µm	20	1	30	4.32	9	7	30-120-20-120	4, 10, 14
L3µm				0.44	28	23	120-300-120-300	

The process was operated at 1 bar and 30°C (**Table 2**) with a flow rate of 1 L/min, corresponding to ~3.5 cm/s. In the beginning of each experiment, 20 grams of sample powder was placed inside the column. Detailed experimental conditions are given in Table 2. To calculate the precursor dosing times, the total amount of active sites in the bed of particles was estimated, *i.e.*, the dangling bonds such as hydroxyl groups. This amount was calculated from the measured BET specific surface area (SSA), the mass of the substrate particles placed inside the column, and the surface concentration of the active groups. The maximum number of TMA molecules that could attach to the surface of the substrate particles was estimated to be around 5 per nm^2, according to the model given by Puurunen et al.[254] The details for the calculation were indicated previously.[7] After dosing each precursor to the reactor, the system was purged with N_2 to remove the excess precursors, establishing a feeding sequence of TMA–N_2–O_3(or H_2O)–N_2. To ensure a full saturation of all the powder inside the column, excess dosing time (3-5 times higher than the calculated values) was applied. The coating was performed for 4, 10 and 14 ALD cycles (Table 2). At the end of each cycle, the reaction was stopped and around 25-30% of the initial powder mass was taken from the column and stored for further characterization. For the remaining powder, the ALD process was continued with the same cycle sequence.

2.3. Surface characterization by transmission electron microscopy (TEM)

The conformality of the alumina coating was investigated via transmission electron microscopy (TEM) and scanning transmission electron microscopy (STEM). The particles were suspended in ethanol and transferred to regular TEM grids (3.05 mm in diameter). TEM and STEM images were taken using a JEOL JEM1400 operating at 120 kV and a FEI Cs corrected cubed Titan operating at 300 kV, respectively. In STEM, the images were obtained in high-angle annular dark-field (HAADF) mode. In parallel with HAADF imaging, energy dispersive X-ray spectroscopy (EDX) measurements were acquired using an Oxford Instruments X-MaxN100TLE detector. Elemental maps of Al and O were collected at several locations on the grids. The TEM images were then analysed using the software package ImageJ to determine the thickness of the alumina film. For each sample, more than 15 particle agglomerates were characterized by measuring the film thickness at multiple places of each particle. The data points shown in the thickness distributions in Figures 5 and S8 represent the average thickness for each particle agglomerate. Instead, the data points shown in Figures S2c-f represent the total average thickness within the whole sample.

2.4. Surface characterization by time of flight secondary-ion mass spectrometry (TOF-SIMS)

The uniformity of alumina deposition was analyzed by time-of-flight secondary ion mass spectrometry (ToF-SIMS). A TOF-SIMS[5] instrument (ION-TOF GmbH, Münster, Germany) equipped with a single-stage reflection analyzer and a bismuth liquid metal ion gun was used to analyze the elemental and molecular information from the outermost layer (typically 1-4 nm) of the surface of the particles. The analysis was conducted in high spatial resolution mode (~200 nm spot size) with Bi_3^+ primary ions. The primary ion gun energy was 30 keV. ToF-SIMS analysis was performed on reference and ALD surface modified lactose particles for areas of 500µm × 500 µm, with 2048 × 2048 pixels. Five scans (i.e. 5 pulses, and therefore 5 spectra) were performed on each pixel. The spectra were calibrated using the CH_3^+, $C_2H_5^+$ and $C_3H_5^+$ fragment ions. The colors show the overlap of the mapping of background tape

(blue), aluminium (from the alumina film, red) at mass 26.98, and lactose (green) with typical mass of fragments at 73.03. 127.04. 145.05. 163.07[26] and lactose plus Na at 365.11 and lactose plus K at 381.09. It should be noted that TOF-SIMS has a limitation of analysis depth. For films that are ultrathin, typically < 1 nm, the signals from the alumina film may be "diluted" by elements from the substrate.

2.5. Elemental analysis by inductively coupled plasma - optical emission spectroscopy (ICP-OES)

Elemental analysis was carried out using ICP-OES (PerkinElmer Optima 2100, PerkinElmer, Waltham, MA, USA). Before measurement, 8-15 mg particles were dissolved overnight in 10 ml acid mixture solutions of H_2O:HNO_3:HOAc in volume ratio of 6:2:2. After destruction, the samples were analyzed with ICP-OES to determine the mass fraction of aluminum in the samples. For each sample, 2-4 replicates were made. From the measured mass fraction of aluminum, the corresponding weight percentage of alumina in the ALD-modified samples was calculated. Based on the weight of Al_2O_3, the measured BET surface area (SSA, m^2/g) and the reported density of the amorphous thin film ($d_{Al_2O_3}$= 2.5 g/cm^3),[27] the thickness of the alumina layer could be calculated as given in our previous work.[7]

2.6. Solid state and materials characterization

2.6.1. X-ray powder diffraction (XRPD)

Structural characterization of the particles was made by XRPD (X'Pert PRO PANalytical Ltd., Nottingham, United Kingdom) through a 12 minutes fast scan program at 45 keV, 40 mA within 2θ 0 - 50°. For each sample 2-3 parallel samples were measured.

2.6.2. Solid state nuclear magnetic resonance (ssNMR)

Solid-state ^{13}C CP/MAS NMR spectra were acquired using a Bruker 400 UltraShield spectrometer (Bruker BioSpin, MA, USA) operating at 100 MHz for ^{13}C. Powder samples (~100 mg) were spun at 9

kHz in a 4 mm ZrO_2 rotor sealed with Kel-F endcaps. Acquisition was performed using a standard sequence with acquisition time 0.0669439 s, 20 s delay and 2 ms contact time and number of scans 1024.

2.7. Surface morphology by scanning electron microscopy and energy dispersive x-ray (SEM/EDX)

The morphology of the particles was observed by SEM (FEI Quanta 200) at 15 keV under high vacuum mode. Before observation, the samples were coated with thin film of Au for 150 – 200 s using Cressington sputter coater (108 auto, Watford, United Kingdom). Elemental analysis for the chemical composition on the surface of some particles was carried out using Energy Dispersive X-ray (EDX) analyzer INCA Penta FETx3 (Oxford Instruments, Oxfordshire, United Kingdom), equipped with the SEM.

2.8. Particle Size Distribution by laser diffraction particle sizing (PSD)

The particle size distribution of the particles was measured by laser diffraction particle sizing instrument for dry particles, Mastersizer 2000 (Malvern Instruments Ltd., Worcestershire, United Kingdom). For each sample, 5-8 parallel tests were carried out at a pressure of 3 bar.

2.9. Thermal properties by Thermal Gravimetric Analysis (TGA)

The thermal properties of the particles during heat treatment was observed by TGA (Q500, TA Instrument, New Castle, DE, United States) under N_2 atmosphere by ramping from 25°C to 250°C. Around 5-10 mg particles were used for each test and 1 - 4 duplicates were run for each sample. Some particles after heating to 250°C were observed by SEM.

2.10. Dispersibility in suspension by Focused Beam Reflectance Measurement (FBRM)

The dispersibility of the lactose particles in suspension was monitored inline by a FBRM probe (LASENTEC S400, Mettler Toledo, OH, USA) during mixing of 600±5 mg sample in 600 ml ethanol (99.5%) in a USP2 dissolution apparatus vial (DISTEK Premiere 5100, NJ, USA) with a stirring rate of

150 rpm at room temperature. As a reference, unmodified lactose was tested also with the addition of 0.08% of sodium dodecyl sulfate (SDS) to the ethanol medium.

2.11. Dissolution Measurements

The dissolution tests of the lactose particles were carried out in 80% ethanol in a 100 ml glass vial with stationary rotation of 190 rpm at room temperature (two replicates for each sample). 80% ethanol was used instead of water to dramatically slow down the dissolution rate of the lactose therefore allowing the observation in the initial dissolution stage, i.e. within the first 1-3 min. Prior to the dissolution tests, 50±5 mg of particles was pre-dispersed in 25ml of absolute ethanol with 0.08% SDS for 10 min in order to ensure similar dispersive conditions for all the samples. 20 ml from the upper suspension was then taken for the dissolution test to make a sample concentration of 30±5 mg/ 100 ml. At each time point from 1 to 120 min (1, 3, 5, 7, 9, 12, 20, 30, 60 and 120 min), 1 ml of solution was taken and filtered using a 0.2 μm syringe filter (Millex®). The filtered solutions were analyzed by UPLC (ultra-performance liquid chromatography, Acquity™, Waters, MA, USA) with a charged aerosol detector (CAD, Dionex Coron Veo RS, Thermo Scientific, MA, USA).

3. RESULTS AND DISCUSSION

3.1. Morphology and crystallinity of lactose particles

Alumina nanoscale films were deposited on two kinds of lactose particles, namely milled lactose, Lactohale® 201 (L20μm), and micronized lactose, Lactohale® 300 (L3μm). Both the lactose particles exhibit a broad particle size distribution (PSD) (Figure 1a). In particular, L20μm shows a broader PSD, i.e., from 0.1 to 100 μm (d_{50} =21 μm), than L3μm, whose PSD spans from 0.1 to 20 μm (d_{50} =3.5 μm). Moreover, both lactose grades have complex and irregular particle shapes, arising from the size-reduction processes (Figures 1c-d). Because of their different particle size, the BET specific surface areas of L20μm and L3μm are 0.44 and 4.32 $m^2\ g^{-1}$, respectively. The t-plot method is used to determine whether the

lactose particles contain micropores, i.e. pores less than 2 nm.[28] In case a relatively small fraction of micropores is present, the y-intercept of the t-plot is positive and correlates to the micropore volume. For L3µm, the t-plot suggests the presence of micropores, with a volume of 0.193 $mm^3\ g^{-1}$ (Figure S1). The external surface area, which can be derived from the slope of the t-plot, is estimated to be 4.08 $m^2\ g^{-1}$. Micronization induces the randomized onset of amorphous regions on the surface of the particles, which is reflected in the presence of superficial micropores. Due to high pressures used in the micronization process, such amorphous surfaces are inherently inhomogeneous within and across the particles.

To characterize the crystallinity of the two lactose particles, Thermal Activity Monitor (TAM) measurements (TAM III, TA Instruments, Sollentuna, Sweden) were performed at 25°C under a RH of 75% using a parafilm with a small cavity in the center to cover the sample tube (Figure 1b). Around 150 mg powder was used and two parallel tests were carried out for each sample. During the TAM measurement, the sample is recrystallized by the moisture absorbed during the exposure to NaCl saturated solution (75% RH), and the enthalpy of recrystallization is then related to the degree of amorphicity. For L20µm, the TAM profile does not present any peak, thus indicating a fully crystalline structure. Instead, for L3µm it shows a broad peak between 0 to 5 hours of the measurement. The integrated heat flow, which represents the enthalpy induced by the recrystallization, correlates to an amorphicity of around 5-7%. Amorphous structures are far more hygroscopic than their crystalline counterparts. Therefore, the Al_2O_3 growth may be affected by the different crystallinity and surface chemistry of L20µm and L3µm.

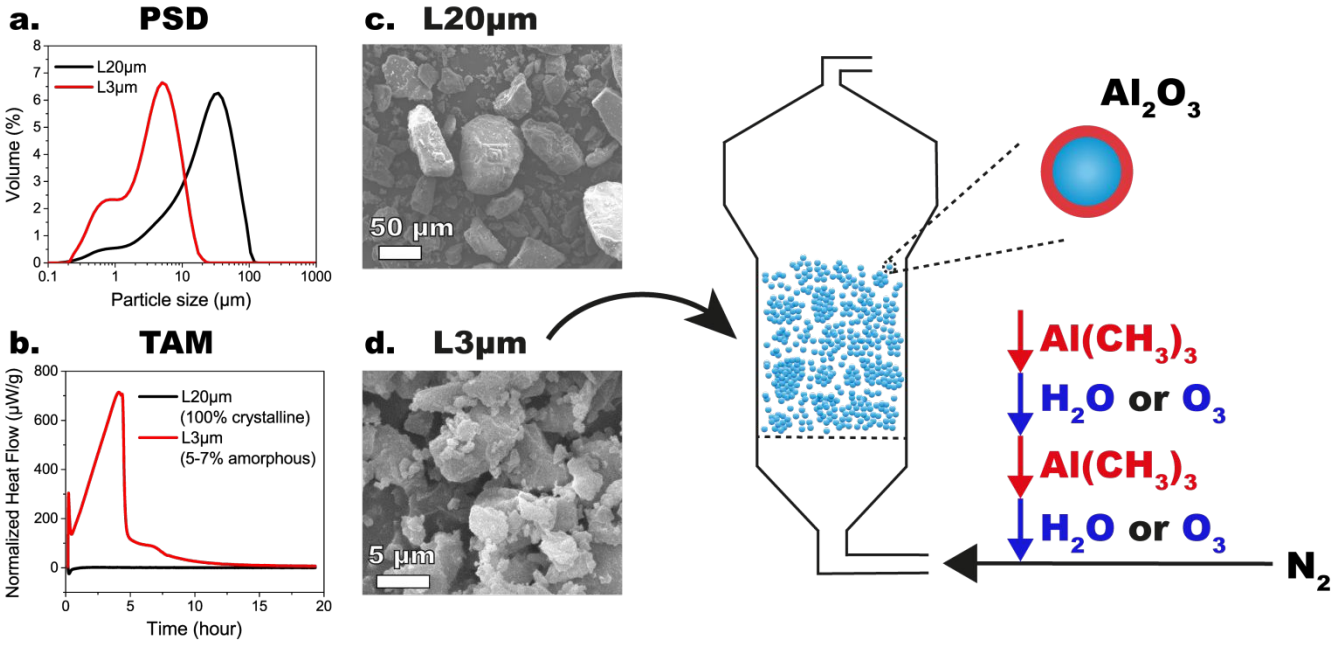

Figure 1: On the left side, morphology and crystallinity of L20µm and L3µm particles. (a) Particle size distributions. (b) TAM profiles. The TAM tests were held at 25°C under an RH of 75% using a parafilm with a small cavity in the centre to cover the sample tube. (c-d) SEM images. On the right side, scheme of the ALD process in a fluidized bed reactor for Al_2O_3 coating.

3.2. Evolution of Al_2O_3 loading with the number of ALD cycles

The amount of deposited Al_2O_3 on L20µm and L3µm was monitored as a function of the number of ALD cycles by ICP-OES. The Al_2O_3 loading increases linearly with the number of cycles for both L20µm and L3µm (Figure 2). As expected, the Al_2O_3 weight percentage (wt. %) is higher on L3µm than on L20µm, given the higher available surface area of the former (Figure 2a). In particular, for L3µm, TMA/O_3 ALD results in slightly higher loadings than those from TMA/H_2O ALD. Instead, for L20µm, both the co-reactants, i.e. H_2O and O_3, lead to similar loadings. To verify whether the Al_2O_3 loading per unit surface area is comparable on L20µm and L3µm, the Al_2O_3 wt. % were re-scaled with respect to their BET specific surface area (Figure 2b). All the loadings collapse close to a single straight line, thus underlining the control over the amount of deposited material regardless of the substrate surface area. Based on the Al_2O_3 wt. %, the BET surface area and the density of the amorphous alumina film, the thickness of the alumina film was estimated (see Table S1 and Figure S2). Before discussing how the estimated thickness

fits with the actual thickness, a quantitative and qualitative analysis of the coating uniformity and conformality is presented.

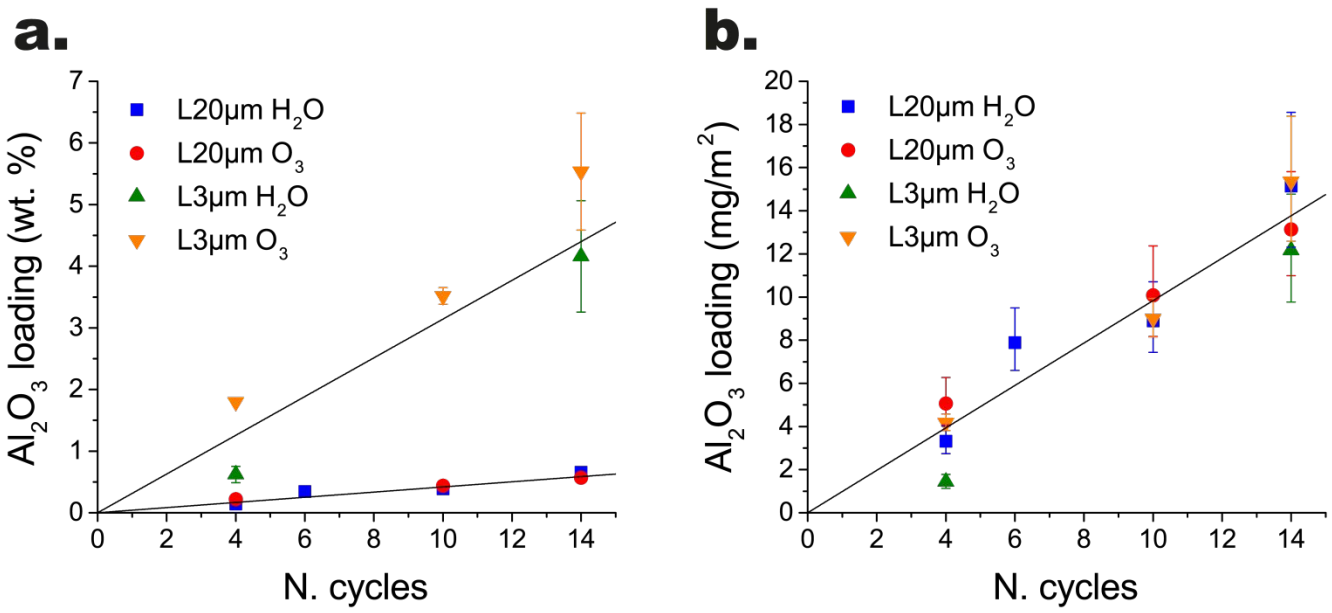

Figure 2: Al_2O_3 loading on both L20µm and L3µm based on ICP-OES analysis as a function of the number of ALD cycles expressed as a) wt.% and b) as mg per unit surface area (m^2). The error bars indicate 95% confidence intervals.

3.3. Effect of co-reactants (H_2O vs O_3) and nature of the substrate on the coating uniformity and conformality

The main advantages of ALD are the uniformity and conformality of the deposited films. The effect of ALD co-reactants, i.e. H_2O and O_3, and of the nature of the substrate, i.e. particle size and crystal structure, on the coating uniformity and conformality were studied. The uniformity and conformality are evaluated by ToF-SIMS and TEM analysis, respectively. ToF-SIMS shows the elemental mapping of aluminum at the micrometer scale, thus allowing the simultaneous detection of alumina films across multiple particles. TEM, instead, enables the visualization of the alumina films at the nanoscale, in other words only on the individual particles. Therefore, TEM lends itself more to the analysis of conformality than of uniformity.

As to ALD on L20µm, ToF-SIMS images show an evident difference between the H_2O-based and the O_3-based process (Figure 3). The use of H_2O as a co-reactant leads to a non-uniform deposition, as

indicated by the large green areas corresponding to the bare lactose particles. Instead, the use of O_3 results in a fully uniform deposition, as shown by the presence of aluminum – in red – on every particle. This is confirmed also by TEM analysis. In the H_2O-based process, both unmodified and modified particles are observed, even after 14 cycles (Figures 3a-c and S3). Instead, for TMA/O_3 ALD each individual particle is uniformly coated, even after only 4 cycles (Figures 3d-f and S4). Despite such a disparity in the coating uniformity, we showed that the H_2O-based process displays comparable Al_2O_3 loadings as the O_3-based one. The reasons behind it lie in the lack of conformality and in the formation of Al_2O_3 nanoparticles in TMA/H_2O ALD (Figures 3a-c, S3 and S5). In fact, the use of H_2O as a co-reactant at room temperature brings about two major drawbacks: i) problems in the purging step and thus possibility of CVD reactions, and ii) deterioration of fluidization. At ambient conditions, the purging step is likely to be ineffective in removing the unreacted water molecules. In particular, if water is overexposed (i.e. 30 s) to the particles, as in this case, and the purging step is not long enough (i.e. 2 min), water will be present both in the vapor-phase and on the surface. Therefore, during the subsequent TMA pulse, gas-phase CVD reactions can occur with water vapor, resulting in the formation of Al_2O_3 nanoparticles. Moreover, water deteriorates the fluidization quality of hygroscopic particles, e.g., lactose, by causing the formation of large agglomerates. At atmospheric conditions, the coating process may be limited by the diffusion of the precursors in the large agglomerates.[298] Therefore, diffusion limitations result in an inhomogeneous coating, or in other words in non-conformal films.

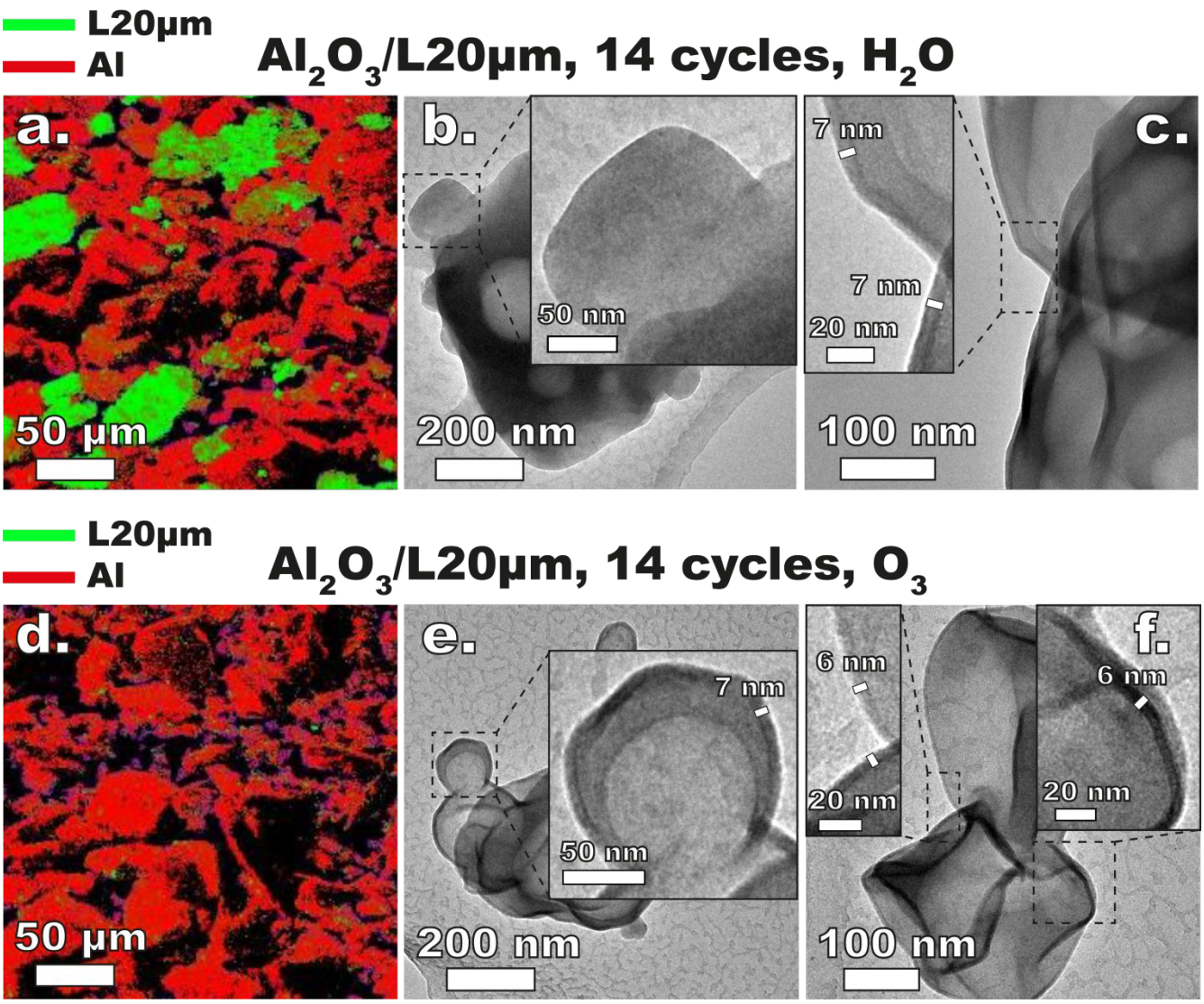

Figure 3: a), d) ToF-SIMS and b, c, e, f) TEM images of Al_2O_3-modified L20µm particles after 14 cycles using H_2O or O_3 as co-reactants. ToF-SIMS micrographs show the overlap of the elemental mapping on the outermost layer (typically 1-4 nm) of the surface of L20µm particles. The colors represent the different components: green- L20µm, red-aluminum, black-background tape.

TEM observations display a broad distribution of Al_2O_3 thickness in H_2O-based ALD on L20µm (Figures 5a and S8a). Without considering the unmodified particles, the coating thickness for the modified particles ranged from ~3.5 nm to 11 nm. Instead, O_3-based ALD on L20µm delivers narrow thickness distributions, ranging from ~5 nm to ~7.5 nm, thus underlining the benefit of O_3 in providing uniform and conformal coatings. To understand whether the observed thickness under TEM is consistent with the

Al_2O_3 loading measured by ICP, the thickness of the alumina film resulting from the Al_2O_3 wt. % was calculated. For L20µm, the calculated thickness is slightly higher than the mean thickness observed under TEM (Figures S2e). It is worth noting that in the calculation the density of the amorphous alumina film is assumed to be 2.5 g/cm^3.[27] The small discrepancy between the calculated and measured film thickness can be attributed to a slightly lower alumina density. In fact, by fitting the alumina density as a parameter in Equation 3 and using the thickness observed under TEM as $t_{Al_2O_3}$, an alumina density of ~2.1±0.4 g/cm^3 was obtained:

$$t_{Al_2O_3} = \frac{d_{lactose}}{2}\left(\sqrt[3]{\frac{x_{Al_2O_3}\ \rho_{lactose}}{1 - x_{Al_2O_3}\rho_{Al_2O_3}} + 1} - 1\right) \qquad \textit{Equation 3}$$

where $d_{lactose}$ is the particle diameter estimated from BET, $x_{Al_2O_3}$ is the Al_2O_3 mass fraction, $\rho_{lactose}$, $\rho_{Al_2O_3}$ are the densities of lactose and amorphous alumina film, respectively. The measured thickness of the alumina film against the number of cycles follows the same trend as the Al_2O_3 loading, as expected (Figures S2a and S2c). In particular, the thickness linearly increases with the number of ALD cycles. By the slope of the trend lines, the growth per cycle (GPC) at the very first stages of the growth can be estimated. For both the H_2O-based and the O_3-based processes, an average GPC of around ~0.5 nm is obtained. The obtained GPC is higher than the GPC reported in literature for ALD of Al_2O_3, which is typically in the range of 0.1-0.2 nm. However, Hyde et al. demonstrated that Al_2O_3 ALD on cellulose cotton fibers exhibits a GPC of ~0.5 nm over the first 50-100 cycles.[30] This excess growth was ascribed to the water absorbed in the cotton before the ALD process which then reacts with TMA. Moreover, it is known that higher GPCs may arise from the higher surface coverage of the precursors throughout ALD at low temperature.[31] Therefore, the GPC of Al_2O_3 on L20µm can be explained by (i) the large amount of water absorbed by lactose, which is extremely hygroscopic,[32] and (ii) the low efficacy of the purging steps at ambient conditions, which lead to additional growth of Al_2O_3 by CVD.

As to ALD on L3µm, ToF-SIMS micrographs do not show any significant difference between the H_2O-based and the O_3-based process (Figures 4a and 4d). Contrary to L20µm, regardless of the co-reactant, all the L3µm particles are fully coated after 14 cycles, as evidenced by the uniform presence of aluminum – in red. Having a smaller particle size, L3µm has a lower tendency to form large agglomerates during the coating process, thus reducing the diffusion limitations of the precursors. TEM and HAADF analysis confirm the presence of complete films on each single particle (Figures 4b-c, e-g, S6 and S7). Furthermore, the higher concentration of Al and O at the edges of the particle is consistent with a lactose core/Al_2O_3 shell structure as indicated by the EDX analysis (Figures 4h-i). However, in both H_2O-based and O_3-based ALD, the thickness of the alumina films on L3µm is larger than the one on L20µm and significantly varies across the particles (Figures 5b and S8b). In particular, the thickness after 14 cycles ranges from 5 nm to 13.5 nm in TMA/H_2O ALD and from 6 nm to 15.5 nm in TMA/O_3 ALD. Such large alumina thicknesses and broad thickness distributions can be attributed to (1) the poor fluidization quality of L3µm, and (2) the amorphous surfaces of L3µm. As mentioned above, the amorphous surfaces may contain micropores. Moreover, during the ALD process, L3µm dehydrates, as evidenced by ssNMR and XRPD data by the emergence of the same peaks in both the ALD-modified and dehydrated samples (Figures 6 and S10). Dehydration presumably leaves molecular pockets, thus inducing more porosity, as suggested by the slight increase in the BET surface area of TGA-dehydrated L3µm (Table 1). Therefore, the gaseous precursors can penetrate within the dehydration-induced porous surfaces, thus leading to the formation of alumina within the surface, as well as on it. The films will then consist of an Al_2O_3-lactose mixture. Being inherently inhomogeneous within and across the particles, the amorphous surfaces of L3µm inevitably lead to non-conformal films, regardless of the co-reactant used.

The thickness of the film on L3µm, resulting from the Al_2O_3 wt. % by ICP, is significantly lower than the mean thickness observed under TEM (Figure S2f). Therefore, the density of the film on L3µm would be even lower than the one on L20µm, and thus closer to the density of lactose itself. By fitting the film

density as a parameter in Equation 1 and using the thickness observed under TEM as t_{Al2O3}, a film density of ~1.6 g/cm^3 was obtained, consistent with the density of lactose. This confirms the hypothesis that the observed films consist of a mixture of Al_2O_3 and lactose, due to the penetration of the precursors through the additional voids caused by dehydration. Similar to L20µm, the measured thickness of the film as a function of the number of cycles on L3µm follows the same trend as the Al_2O_3 loading (Figures S2b and S2d). The thickness linearly increases with the ALD cycles and GPC of ~0.6 nm and ~0.7 nm are extrapolated for H_2O-based and O_3-based ALD, respectively. Contrary to the deposition on L20µm, TMA/H_2O ALD on L3µm does not lead to any formation of Al_2O_3 nanoparticles. In fact, the contribution of CVD reactions in the gas-phase is higher on lower-surface-area particles, where water molecules are more likely to be present both in the vapor-phase and on the surface, especially for overexposures of water. The higher the surface area, the lower the contribution of CVD in the gas-phase, the less the formation of Al_2O_3 nanoparticles. Therefore, in case of higher-surface-area substrates (e.g., L3µm), water is mostly present on the surface, where TMA reacts during the subsequent pulse, leading only to the formation of Al_2O_3 films.

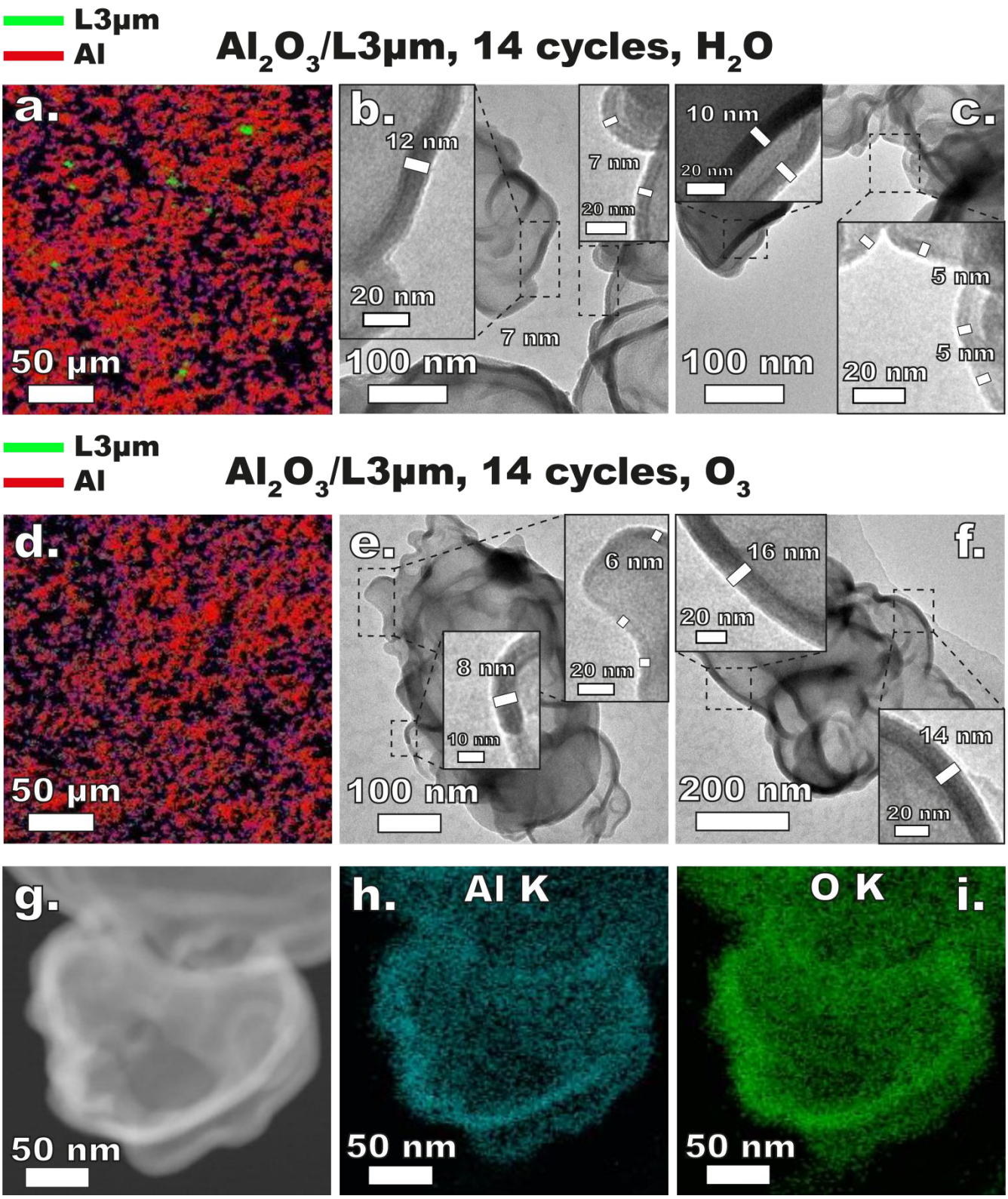

Figure 4: ToF-SIMS, TEM, HAADF images and EDX mapping of Al_2O_3-modified L3µm particles after 14 cycles using H_2O or O_3 as co-reactants. (a, d) ToF-SIMS micrographs show the overlap of the elemental mapping on the outermost layer (typically 1-4 nm) of the surface of L3µm particles. The colors

represent the different components: green- L3µm, red-aluminum, black-background tape. (b, c, e, f) TEM images. (g) HAADF image. (h, i) Al K and O K series of EDX mapping.

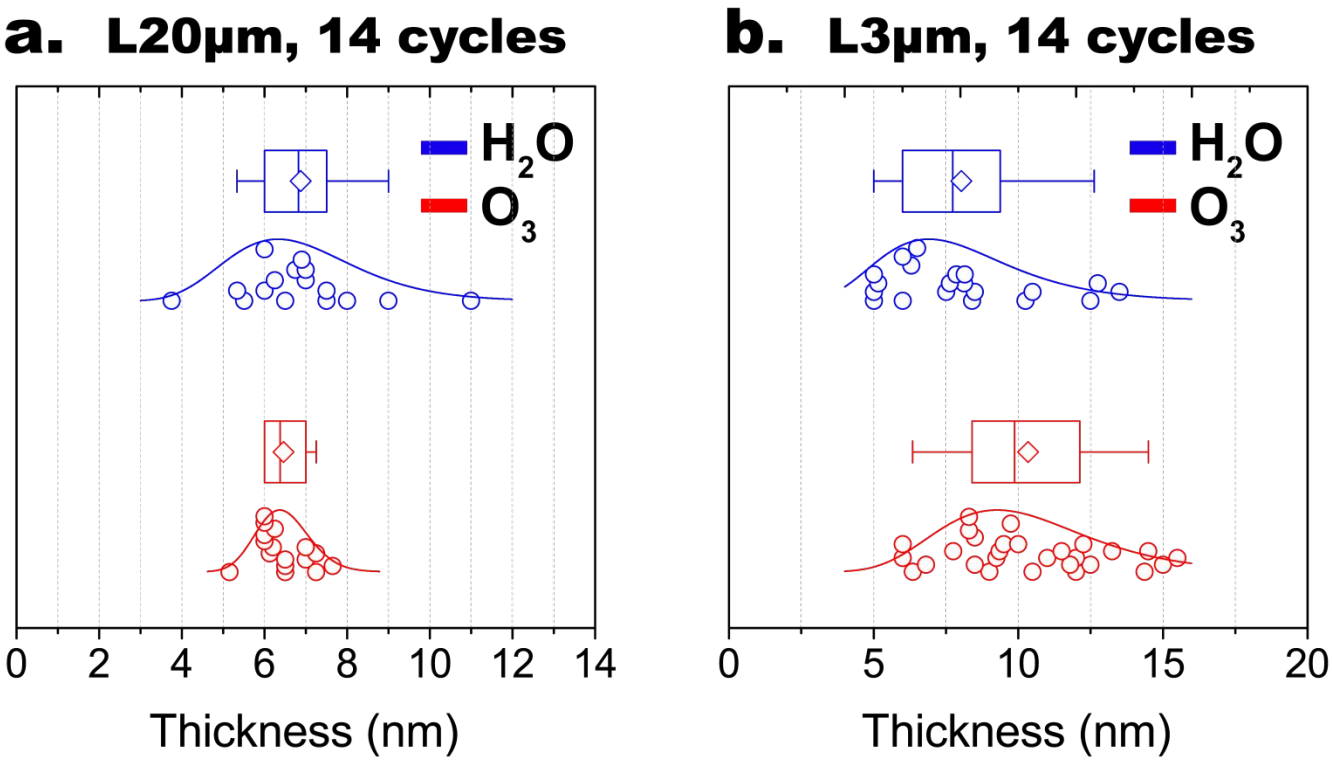

Figure 5: Thickness distribution of the Al_2O_3-modified particles after 14 cycles using either H_2O or O_3 as a co-reactant for (a) L20µm and (b) L3µm. The boxes indicate the 10^{th}, 25^{th}, 50^{th}, 75^{th}, and 90^{th} percentiles of the population, and the white diamonds indicate the average.

3.4. Evaluation of surface modified lactose physical and chemical properties

Both ssNMR and XRPD analysis were used to understand whether the chemical structure (i.e. α-lactose monohydrate) of the lactose particles were stable upon the ALD process (Figures 6, S9 and S10). No decomposition is observed for either L20µm and L3µm particles after ALD within the level of detection. In addition, the UPLC-CAD analysis after the dissolution tests show no extra peaks for the modified particles with both sizes than the bare samples, which confirms the ALD process does not induce decomposition of the lactose when using both co-reactants (Figure S15). The ssNMR spectra show that L20µm (Figure S9) maintains its structure after ALD, whereas L3µm (Figure 6) undergoes dehydration. Compared to the spectrum of unmodified L3µm, the ssNMR spectra of both ALD-modified and

dehydrated (TGA-treated) L3µm exhibit additional peaks, marked by the dashed rectangles, at the same positions (Figure 6). This suggests that the changes in the structure after ALD are due to the dehydration of L3µm. The peak intensity correlates to the degree of dehydration. In particular, the degree of dehydration of ALD-modified L3µm is close to the one of the dehydrated samples with a dehydration degree of 47.5%. The XRPD patterns before and after ALD do not show any major difference, except for the emergence of a small peak at 18°, marked by the dashed rectangle (Figure S10). Garnier et al. found the appearance of the peak at 18° in α-lactose monohydrate upon heating at 100°C.[33] By comparing the diffractograms of ALD-modified and TGA-dehydrated L3µm, it can be concluded that the peak is due to the dehydration of L3µm. The dehydration of L3µm is ascribed to the temperature rising to 60-70 °C temporarily during ALD due to the exothermal reactions of both TMA and the co-reactants with the surface of the particles. Instead, given the lower surface area available and thus the shorter precursor exposure times, the reaction temperature during ALD on L20µm was constant at 30 °C. Therefore, no difference is observed in the ssNMR spectra of unmodified and modified L20µm (Figure S9).

The dehydration of L3µm leads to an increase in the BET specific surface area due to an increase in porosity arising from the removal of water molecules. This is confirmed by the comparison of the BET specific surface areas of unmodified and dehydrated L3µm, where the SSA increases by 15% upon 76% dehydration (Table 1). Raut et al. found that the BET SSA of α-lactose monohydrate increased by 48% after complete dehydration.[33]

After the ALD process, the powder shows different morphologies depending on the co-reactant used. On the one hand, after H_2O-based ALD, both L20µm and L3µm powders contain mm-sized agglomerates, visible to the naked eye (Figure S11). As mentioned above, the formation of large agglomerates is due to water capillary bridges between the lactose particles forming during the coating process. On the other hand, O_3-based ALD delivers fine and well-dispersed powder (Figure S11). Moreover, SEM images do not display any significant difference in the size and morphology of unmodified and modified individual

particles, thus indicating that the agglomeration phenomena occurring during the coating process do not affect the primary particle size (Figures S12c-h).

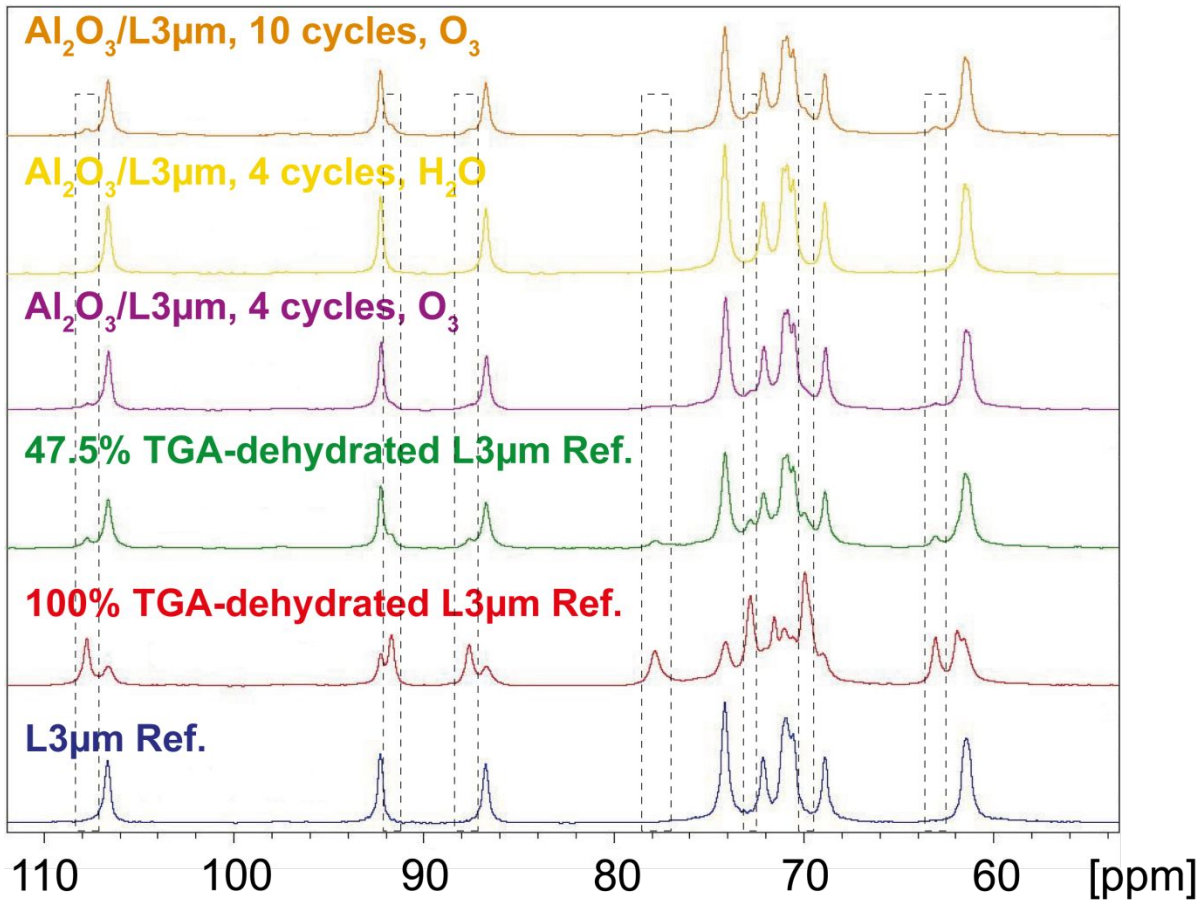

Figure 6. ssNMR patterns of L3µm particles before and after ALD using either H_2O or O_3 as co-reactants, as well as samples after TGA treatment at different degrees of dehydration.

The PSDs of L20µm modified using H_2O as a co-reactant move towards larger sizes (Figure S12a). In particular, the 4-cycle-modified particles exhibit agglomerates ranging from 0.1 to 1 mm, which are no longer present by increasing the number of cycles. As a result, the number of modified particles increases, as observed from the ToF-SIMS micrographs, and thus the cohesive forces between the lactose particles are reduced. In other words, once most of the particles are coated, the agglomeration phenomena are significantly reduced. Therefore, Al_2O_3 ALD effectively prevents agglomeration occurring during the coating process. The PSDs of O_3-processed L20µm do not show any deviation from the one of

unmodified L20µm, thus confirming that no agglomeration takes place. The PSDs of modified L3µm first slightly shift to higher sizes after 4 cycles, and then to smaller ones after 14 cycles, thus underlining the relevance of the coating cycles in mitigating agglomeration at the microscale (Figure S12b). Overall, the range of particle size for both L20µm and L3µm remains nearly unaltered after the coating process, meaning that no aggregates, but rather the single particles are coated.

As shown in the TGA results, both unmodified and modified L20µm and L3µm particles are stable up to around 75 °C (Figures S13a-b) under the experimental conditions. All the modified samples have a higher decomposition rate compared to the unmodified ones. In particular, the higher the number of cycles, the faster the decomposition process. This effect is more pronounced for L3µm particles, given the higher available surface area. Kaariainen et al. ascribed such behavior to the presence of decomposable carbonaceous species in the modified samples.[8] In fact, the use of TMA can result in the formation of carbonaceous species within the film. Furthermore, as we explained in our previous work,[7] during TGA, the particulate structure of the unmodified samples fully disappeared, whereas the modified ones exhibit structures with different degrees of sintering (Figures S13c-d). Therefore, during the heating process, the unmodified particles melt into a single mass, whereas the alumina coating is effective in separating the particles. As a result, the modified particles retain a higher surface area available for effective heat and mass transfer during TGA.

3.5. Evaluation of surface modified lactose on functional properties: dissolution

The effect of Al_2O_3 ALD on the dissolution rate of the lactose particles was investigated in 80% ethanol solutions over 2 hours (Figure 7). The unmodified L20µm particles fully dissolve after 1 h, and the unmodified L3µm ones within 5 min. This is due to the large particle size of L20µm compared to L3µm. The L20µm particles after 4 TMA/H_2O ALD cycles show a similar profile to the unmodified particles, reaching 100% dissolution after 1 h. In fact, as observed from ToF-SIMS and TEM analysis, a large portion of particles are still unmodified in the H_2O-based process. Instead, the L20µm particles after 4

TMA/O_3 ALD cycles take a significantly longer amount of time to dissolve. In particular, the cumulative dissolution slowly reaches ~90% after 1 h. Such a retarding effect is even magnified with the increasing number of cycles. For the 14-cycle-modified L20µm particles, the cumulative dissolution after 1 h is ~80% and 57% in H_2O-based and O_3-based ALD, respectively, thus underlining the benefit of uniform and conformal coatings provided by O_3.

In the case of L3µm, the dissolution profiles of the particles modified by 4 ALD cycles deviate only slightly from the reference one. In particular, the cumulative dissolution after 5 min is 98% and 95% in H_2O-based and O_3-based ALD, respectively, and reaches 100% after ~10 min in both processes. Increasing the number of cycles leads to a significantly reduced dissolution rate. In fact, for the 14-cycle-modified L3µm particles, the cumulative dissolution after 5 min is 60% and 48% for H_2O-based and O_3-based ALD, respectively, and after 2 h reaches 83% for both processes. The initial slower dissolution for the TMA/O_3-modified particles can be ascribed to the slightly thicker films, as shown in Figure 5. Moreover, the particles after 14 TMA/H_2O ALD cycles are not fully dissolved even after 17 h – ~90% cumulative dissolution, thus suggesting a total dissolution over several days. Such a dramatic retardation of dissolution by Al_2O_3 coatings has also been shown by Vogel et al.[35] They impregnated poly(vinyl alcohol) nanofibers with known amount of ketoprofen molecules and then carried out Al_2O_3 ALD for 2, 20 and 200 cycles. The time of total release of ketoprofen in water was 2 min for the uncoated sample, over 24 h for the 2-cycle-coated one, ~9 days for the 20-cycle-coated one and 30-39 days for the 200-cycle-coated one. Since the dissolution rates scale with the number of cycles, or in other words with the coating thickness, it is likely that water accesses the nanofiber through defects or bulk transport through the ALD coating. In particular, they suggest that the release mechanism is due to a combination of water diffusing through and the slow erosion of the ALD coating. Increasing the coating thickness reduces coating defects, thus expanding the distance that water must travel to access the nanofiber. Analogously, the dissolution mechanism of the coated lactose particles is likely to involve the transport of water

through voids in the Al_2O_3 shell. The higher the number of cycles (and higher coating thickness), the slower the solution penetrates through the alumina film, and the slower the lactose dissolution. It is worth noting that already a few ALD cycles (i.e., from 4 to 14), and hence thin alumina films (i.e., from ~2 to ~10 nm in terms of average thickness), induce a significant change in the dissolution performance. Therefore, Al_2O_3 thin films provide an efficient dissolution barrier for the lactose particles.

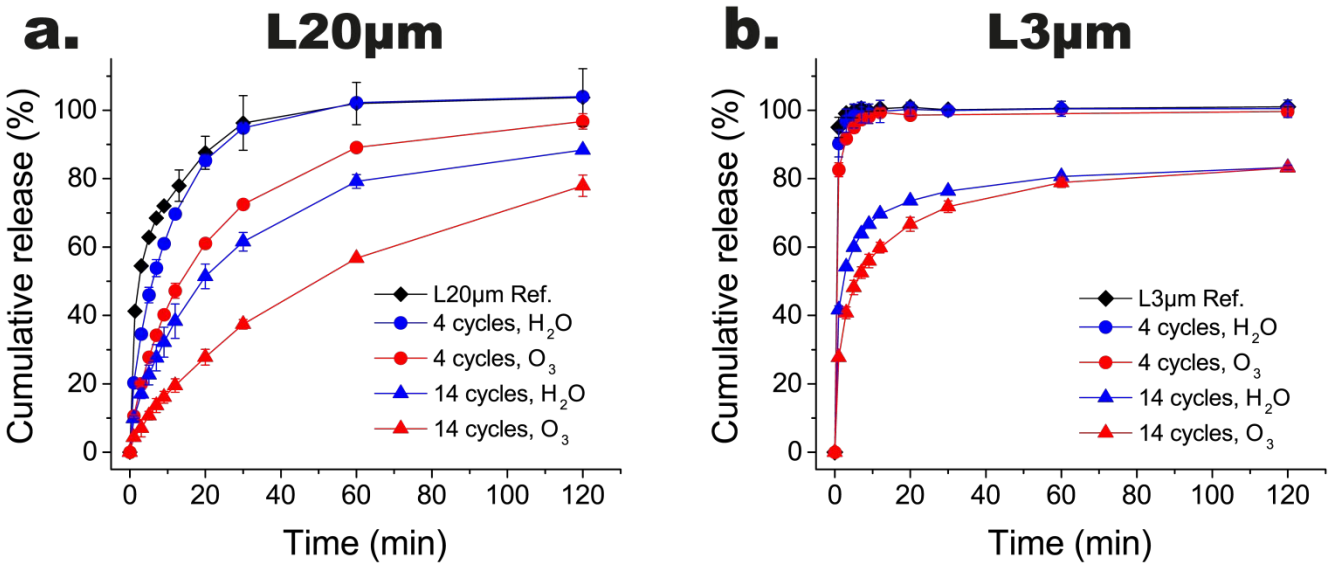

Figure 7. Dissolution profiles in 80% EtOH over 2 hours after pre-dispersion in EtOH + 0.08% sodium dodecyl sulfate (SDS) for 10 min of (a) L20µm and (b) L3µm particles. The error bars indicate 95% confidence intervals.

3.6. Evaluation of surface modified lactose on functional properties: dispersibility

To study the effect of ALD on the dispersibility of the lactose particles in liquid phase, focused beam reflectance measurements (FBRM) were performed for L3µm. Lactose has a negligible solubility in pure ethanol, and therefore the dispersibility of the particles in ethanol can be characterized without being affected by the solubilization of the particles. The number of unmodified and modified L3µm particles in different size ranges (i.e., 1-5, 5-10, 10-20, 20-100 and 100-1000 µm) were measured over 15 min (Figures 8 and S14). The higher the number of particles in the range 1-10 µm, which is the actual size range of L3µm, the better the dispersibility. Vice versa, the higher the number of large agglomerates, i.e.

100-1000 µm, the poorer the dispersibility. After about 10 min, each particle size range of each sample flattens out, indicating that the suspension reaches a steady state. On the one hand, the number of particles in the size range of 1-10 µm significantly increases with the ALD cycles (Figure 8a). In particular, while it stays constant for the 4-cycle-modified samples, it becomes more than twice as high for the 14-cycle-modified ones. On the other hand, the number of particles in the size range of 100-1000 µm significantly decreases with the ALD cycles (Figure 8b). Moreover, by having a closer look at the evolution with time, it can be seen that the number of particles of 1-10 µm for both unmodified and 4-cycle-modified L3µm slightly increases from 1 to 10 min likely due to the breakage of the larger agglomerates, whereas for 14-cycle-modified L3µm it decreases likely due to the detachment of particles smaller than 1 µm. Instead, the number of particles of 100-1000 µm for both unmodified and modified L3µm decreases from 1 to 10 min, due to the breakage of the soft agglomerates within the samples.

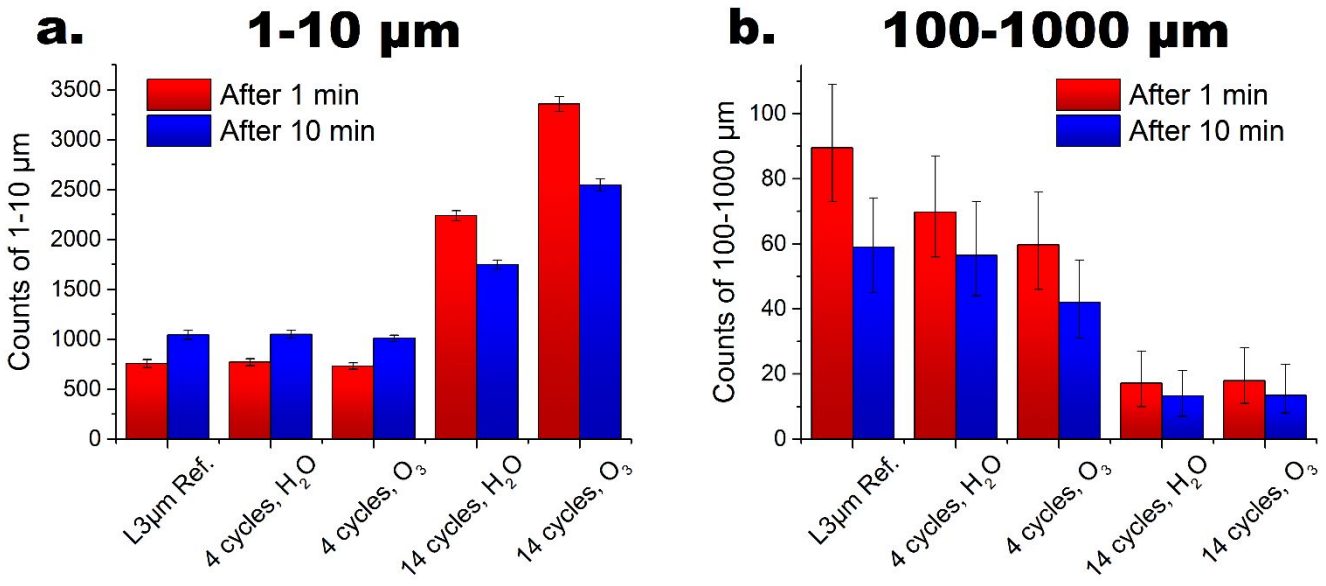

Figure 8: Number of particles for the Al_2O_3/L3µm samples in the size range of a) 1-10 µm and b) 100-1000 µm measured by a Focused Beam Reflectance Measurement (FBRM) probe after 1 and 10 min in 99.5% EtOH showing the dispersibility of the particles in the liquid phase. The error bars indicate 95% confidence intervals.

The amorphous structure in L3µm leads to high surface energy and thus resulting in cohesive powders with tendency to form agglomerations in liquid media. To understand the influence of the amorphicity on the properties of the L3µm, some of the particles were recrystallized under conditions at RH 54% for 24 hours. The TAM analysis showed no peak which indicates the removal of the amorphicity in the recrystallized samples. As seen in Figure S14, the FBRM patterns of the recrystallized sample of L3µm show a much better particle dispersibility in the initial stage than the original sample containing amorphicity. The crystalline L3µm exhibits improved homogeneity and stability in the surface properties thus resulting in a reduced tendency of initial agglomeration in suspension.

The presence of large agglomerates in the unmodified and 4-cycle-modified samples indicates strong inter-particle forces of the bare lactose particles. Increasing the number of ALD cycles, and thus the coating thickness, significantly modifies the surface properties, which then depend on the coating material rather than on the underlying particles. Specifically, smooth Al_2O_3 films are very hydrophilic, thus improving the wettability of the particles.[36] Such a behavior in pure ethanol is also found in 80% ethanol solution, used for the dissolution tests. Overall, the L3µm particles after 4 ALD cycles show similar dispersibility to the ones of unmodified L3µm, whereas the particles after 14 ALD cycles exhibit considerably improved dispersibility.

4. DISCUSSION AND FUTURE WORK

A comparison of ozone and water as co-reactants for ALD processing and engineering high quality conformal coatings on pharmaceutical particles has been studied. In addition, the effect of lactose substrate particle size and the impact of particle surfaces (crystalline vs. amorphous) was characterised in depth for fully crystalline lactose, L20µm and crystalline lactose with micronization-induced amorphous surfaces, L3µm. The amount of deposited alumina per unit area is similar for both L20µm and L3µm, regardless of co-reactant, and linearly increases with the number of cycles, thus highlighting

the efficient control of ALD over the amount of synthesized material. Overall, modified functional properties for the nano-thin coated particles have been successfully achieved and demonstrated with physical and chemical characterisation.

ToF-SIMS and TEM images show that for crystalline lactose (L20µm) O_3-based ALD offers greatly improved control over the coating uniformity and conformality compared to H_2O-based ALD. In fact, the use of H_2O as a co-reactant during fluidization of lactose particles results in the formation of large agglomerates which may limit the diffusion of the gaseous precursors, thus leading to non-uniform and non-conformal films. TEM image analysis of alumina modified crystalline lactose (L20µm) revealed that H_2O-based ALD delivers broad thickness distributions, whereas O_3-based ALD gives narrow ones.

On the other hand, the H_2O-based and O_3-based processes deliver uniform, but not conformal films on amorphous lactose surfaces (L3µm). The thickness of the alumina films on L3µm is larger than the one on crystalline lactose (L20µm) and significantly varies between individual particles. The lack of conformality on L3µm can be ascribed to the poorer fluidization quality and the presence of amorphous structures at the surfaces. The amorphous surfaces of L3µm present microporosity, which will increase during the ALD process due to dehydration of L3µm for which evidence was provided by ssNMR and XRPD. Hence, the gaseous precursors can penetrate within the dehydration-induced porous surfaces, thus leading to the formation of films consisting of an Al_2O_3-lactose mixture. The micronisation-induced amorphous surfaces of L3 particles are already expected to be inhomogeneous within particles due to the irregular particle surfaces and high energies used in the micronization processes. Therefore, this inevitably leads to non-conformal films, regardless of the co-reactant used for L3 particles.

The dissolution rates of the modified particles were significantly reduced by increasing the alumina film thickness. The L20µm particles modified by O_3-based ALD dissolved much slower than the ones modified by H_2O-based ALD, thus underlining the benefit of uniform and conformal coatings provided by O_3. Instead, the L3µm particles modified by O_3-based ALD show only an initial slower dissolution

compared to the ones modified by H_2O-based ALD due to the slightly thicker alumina films. Moreover, the 14-cycle-modified L3µm particles exhibit considerably better dispersibility compared to the unmodified particles.

The ALD technology used in these studies is based on a fluidized bed reactor that is conducted in the dry state. The successful results using ozone as a co-reactant opens opportunities for the modification of surface properties of humidity- and temperature-sensitive APIs and excipients with particle sizes across the upper nano- to micro-meter lengths. One novel application of ALD can be for nano-engineering of APIs for inhaled drug delivery, where drug particles with an aerodynamic diameter smaller than 5 µm are required for lung deposition. Stabilization of sensitive particles and high energy solid forms (e.g. salts, amorphous forms and metastable polymorphs) with a conformal outer thin film is an attractive prospect for both drug product manufacturing and maximising shelf-life. As an example, this holds prospects for advancing inhaled drug delivery through increasing the diversity of APIs for dry powder inhaler administration. In addition, aerolisation of inhaled particles from Inhalers is dependent on the choice of inhaler and patient lung capacity, as well as attachment/detachment of API particles from carrier excipient particles. The detachment of drug particles from carrier particles is strongly controlled by the physicochemical particle properties, including size, shape, and surfaces[37]. Most particle engineering approaches alter particle properties such as size, shape and surface energy[38]. ALD as demonstrated here is a technology that that does not alter particle size or shape and can be applied also to carrier particles (usually lactose). More importantly, nano-engineering of inhalable particles and modification of surface properties provides less cohesive powders with improved aerolisation properties thereby ensuring more drug may reach the lung. Carrier-free inhaled formulations are, therefore, highly prospective and would reduce manufacturing costs and complexity, whilst potentially offering "tailorable" aerolisation properties through coating material and thickness. The results in this study also emphasize

the importance of advanced material analytical techniques to enable in-depth characterization and understanding of surface modifications of organic particles also at the atomic level.

In summary, ALD is a highly promising technique for generating more complex materials for applications such as novel drug delivery, as well as improved functionality for novel applications in the pharmaceutical, medicine, biological and advanced materials areas

5. SUPPORTING INFORMATION

t-plot of uncoated L3µm; Al_2O_3 thickness values from TEM and ICP-OES analysis; ToF-SIMS and TEM images of Al_2O_3-coated L3µm and L20µm particles after 4 and 10 cycles; supplementary Al_2O_3 thickness distributions; ssNMR of L20µm and XRPD of L3µm before and after ALD; digital photos, SEM images, PSDs and TGAs of both L20µm and L3µm powders before and after ALD.

6. FUNDING

Funding for all researchers was provided by AstraZeneca AB and Health Holland (DLaZ and RvO).

7. ACKNOWLEDGEMENT

Mr. Mark Nicholas (AstraZeneca) is especially acknowledged for TOF-SIMs measurements and data analyses. Ms. Mojgan Talebi is acknowledged for her assistance in part of the coating experiments. This work was funded by AstraZeneca.

8. REFERENCES

1. Sun, C. C. Materials Science Tetrahedron--a Useful Tool for Pharmaceutical Research and Development. *J. Pharm. Sci.* **2009,** *98*, 1671-1687.
2. Martinson, A. B. F.; DeVries, M. J.; Libera, J. A.; Christensen, S. T.; Hupp, J. T.; Pellin, M. J.; Elam, J. W. Atomic Layer Deposition of Fe_2O_3 Using Ferrocene and Ozone. *J. Phys. Chem. C* **2011,** *115*, 4333-4339.
3. Valdesueiro, D.; Prabhu, M. K.; Guerra-Nunez, C.; Sandeep, C. S. S.; Kinge, S.; Siebbeles, L. D. A.; de Smet, L. C. P. M.; Meesters, G. M. H.; Kreutzer, M. T.; Houtepen, A. J.; van Ommen, J. R. Deposition Mechanism of Aluminum Oxide on Quantum Dot Films at Atmospheric Pressure and Room Temperature. *J. Phys. Chem. C* **2016,** *120*, 4266-4275.

4. Wang, F.; Zhang, Y.; Chen, X.; Leng, B.; Guo, X.; Zhang, T. ALD Mediated Heparin Grafting on Nitinol for Self-expanded Carotid Stents. *Colloids Surf., B* **2016,** *143*, 390-398.
5. Ras, R. H. A.; Kemell, M.; de Wit, J.; Ritala, M.; ten Brinke, G.; Leskelä, M.; Ikkala, O. Hollow Inorganic Nanospheres and Nanotubes with Tunable Wall Thicknesses by Atomic Layer Deposition on Self-Assembled Polymeric Templates. *Adv. Mater. (Weinheim, Ger.)* **2007,** *19*, 102-106.
6. Ferguson, J. D.; Weimer, A. W.; George, S. M. Atomic Layer Deposition of Al_2O_3Films on Polyethylene Particles. *Chem. Mat.* **2004,** *16*, 5602-5609.
7. Zhang, D.; Quayle, M. J.; Petersson, G.; van Ommen, J. R.; Folestad, S. Atomic Scale Surface Engineering of Micro- to Nano-sized Pharmaceutical Particles for Drug Delivery Applications. *Nanoscale* **2017,** *9*, 11410-11417.
8. Kaariainen, T. O.; Kemell, M.; Vehkamaki, M.; Kaariainen, M. L.; Correia, A.; Santos, H. A.; Bimbo, L. M.; Hirvonen, J.; Hoppu, P.; George, S. M.; Cameron, D. C.; Ritala, M.; Leskela, M. Surface Modification of Acetaminophen Particles by Atomic Layer Deposition. *Int. J. Pharm.* **2017,** *525*, 160-174.
9. Hautala, J.; Kaariainen, T.; Hoppu, P.; Kemell, M.; Heinamaki, J.; Cameron, D.; George, S.; Juppo, A. M. Atomic Layer Deposition-A Novel Method for the Ultrathin Coating of Minitablets. *Int. J. Pharm.* **2017,** *531*, 47-58.
10. Hellrup, J.; Rooth, M.; Johansson, A.; Mahlin, D. Production and Characterization of Aluminium oOide Nanoshells on Spray Dried Lactose. *Int. J. Pharm.* **2017,** *529*, 116-122.
11. Mirvakili, M. N.; Bui, H. V.; van Ommen, J. R.; Hatzikiriakos, S. G.; Englezos, P. Enhanced Barrier Performance of Engineered Paper by Atomic Layer Deposited Al_2O_3 Thin Films. *ACS Appl. Mater. Interfaces* **2016**, *8*, 13590-13600.
12. Valdesueiro, D.; Garcia-Triñanes, P.; Meesters, G. M. H.; Kreutzer, M. T.; Gargiuli, J.; Leadbeater, T. W.; Parker, D. J.; Seville, J. P. K.; van Ommen, J. R. Enhancing the Activation of Silicon Carbide Tracer Particles for PEPT Applications using Gas-phase Deposition of Alumina at Room Temperature and Atmospheric Pressure. *Nucl. Instrum.Methods Phys. Res.,Sect. A* **2016,** *807*, 108-113.
13. Valdesueiro, D.; Meesters, G. M. H.; Kreutzer, M. T.; van Ommen, J. R. Gas-Phase Deposition of Ultrathin Aluminium Oxide Films on Nanoparticles at Ambient Conditions. *Materials* **2015,** *8*, 1249-1263.
14. Higashi, G. S.; Fleming, C. G. Sequential Surface Chemical Reaction Limited Growth of High Quality Al_2O_3 Dielectrics. *Appl. Phys. Lett.* **1989,** *55*, 1963-1965.
15. Kim, J. B.; Kwon, D. R.; Chakrabarti, K.; Lee, C.; Oh, K. Y.; Lee, J. H. Improvement in Al_2O_3 Dielectric Behavior by using Ozone as an Oxidant for the Atomic Layer Deposition Technique. *J. Appl. Phys. (Melville, NY, U.S.)* **2002,** *92* (11), 6739-6742.
16. Elliott, S. D.; Scarel, G.; Wiemer, C.; Fanciulli, M.; Pavia, G. Ozone-Based Atomic Layer Deposition of Alumina from TMA: Growth, Morphology, and Reaction Mechanism. *Chem. Mat.* **2006,** *18*, 3764-3773.
17. Kim, J.; Chakrabarti, K.; Lee, J.; Oh, K.-Y.; Lee, C. Effects of Ozone as an Oxygen Source on the Properties of the Al_2O_3 Thin Films prepared by Atomic Layer Deposition. *Mater. Chem. Phys.* **2003,** *78*, 733-738.
18. Sundstrom, H. Ozone as the Oxidizing Precursor in Atomic Layer Deposition. *Gas & Chemicals, MKS Instruments Inc* **2005,** (Journal, Electronic).
19. Shen, Y. D.; Li, Y. W.; Zhang, J. Z.; Zhu, X. I. A.; Hu, Z. G.; Chu, J. H. Excellent Insulating Behavior of Al_2O_3 Thin Films Grown by Atomic Layer Deposition Efficiently at Room Temperature. *Optoelectron. Adv. Mat., Rapid Commun.* **2012,** *6*, 5.

20. Cheng, L.; Qin, X.; Lucero, A. T.; Azcatl, A.; Huang, J.; Wallace, R. M.; Cho, K.; Kim, J. Atomic Layer Deposition of a High-K Dielectric on MoS_2 using Trimethylaluminum and Ozone. *ACS Appl. Mater. Interfaces* **2014,** *6*, 11834-11838.
21. Larhrib, H.; Martin, G. P.; Prime, D.; Marriott, C. Characterisation and Deposition Studies of Engineered Lactose Crystals with Potential for use as a Carrier for Aerosolised Salbutamol Sulfate from Dry Powder Inhalers. *Eur. J. Pharm. Sci.* **2003,** *19*, 211-221.
22. van Ommen, J. R.; Valverde, J. M.; Pfeffer, R. Fluidization of Nanopowders: A Review. *J. Nanopart. Res.* **2012,** *14*, 737.
23. Hakim, L. F.; George, S. M.; Weimer, A. W. Conformal Nanocoating of Zirconia Nanoparticles by Atomic Layer Deposition in a Fluidized Bed Reactor. *Nanotechnology* **2005,** *16* (7), S375-S381.
24. Harris, A. T. On the Vibration Assisted Fluidisation of Silica Nanoparticles. *Int. J.Nanotechnol.* **2008,** *5*, 179.
25. Puurunen, R. L. Growth Per Cycle in Atomic Layer Deposition: A Theoretical Model. *Chem. Vap. Deposition* **2003,** *9*, 249-257.
26. Zhou, Q. T.; Denman, J. A.; Gengenbach, T.; Das, S.; Qu, L.; Zhang, H.; Larson, I.; Stewart, P. J.; Morton, D. A. V. Characterization of the Surface Properties of a Model Pharmaceutical Fine Powder Modified with a Pharmaceutical Lubricant to Improve Flow via a Mechanical Dry Coating Approach. *J. Pharm. Sci.* **2011,** *100*, 3421-3430.
27. Groner, M. D.; Fabreguette, F. H.; Elam, J. W.; George, S. M. Low-Temperature Al_2O_3Atomic Layer Deposition. *Chem. Mat.* **2004,** *16*, 639-645.
28. Lowell, S.; Shields, J. E.; Thomas, M. A.; Thommes, M. *Characterization of Porous Solids and Powders: Surface Area, Pore Size and Density*. 1st ed; Springer, Dordrecht, 2004.
29. Grillo, F.; Kreutzer, M. T.; van Ommen, J. R. Modeling the Precursor Utilization in Atomic Layer Deposition on Nanostructured Materials in Fluidized Bed Reactors. *Chem. Eng. J. (Amsterdam, Neth)* **2015,** *268*, 384-398.
30. Hyde, G. K.; Park, K. J.; Stewart, S. M.; Hinestroza, J. P.; Parsons, G. N. Atomic Layer Deposition of Conformal Inorganic Nanoscale Coatings on Three-dimensional Natural Fiber Systems: Effect of Surface Topology on Film Growth Characteristics. *Langmuir* **2007,** *23*, 9844-9849.
31. Liang, X.; Hakim, L. F.; Zhan, G.-D.; McCormick, J. A.; George, S. M.; Weimer, A. W.; Spencer, J. A.; Buechler, K. J.; Blackson, J.; Wood, C. J.; Dorgan, J. R. Novel Processing to Produce Polymer/Ceramic Nanocomposites by Atomic Layer Deposition. *J. Am. Ceram. Soc.* **2007,** *90*, 57-63.
32. Listiohadi, Y.; Hourigan, J. A.; Sleigh, R. W.; Steele, R. J. Moisture Sorption, Compressibility and Caking of Lactose Polymorphs. *Int. J. Pharm.* **2008,** *359*, 123-134.
33. Garnier, S.; Petitsamuel.petit@univ-rouen.fr, S.; Coquerel, G. Dehydration Mechanism and Crystallisation Behaviour of Lactose. *J. Therm. Anal. Calorim.* **2002,** *68*, 489-502.
34. Raut, D. M.; Allada, R.; Pavan, K. V.; Deshpande, G.; Patil, D.; Patil, A.; Deshmukh, A.; Sakharkar, D. M.; Bodke, P. S.; Mahajan, D. T. Dehydration of Lactose Monohydrate: Analytical and Physical Characterization. *Pharm. Lett.* **2011,** *3*, 202-212.
35. Vogel, N. A.; Williams, P. S.; Brozena, A. H.; Sen, D.; Atanasov, S.; Parsons, G. N.; Khan, S. A. Delayed Dissolution and Small Molecule Release from Atomic Layer Deposition Coated Electrospun Nanofibers. *Adv. Mater. Interfaces* **2015,** *2*, 1.
36. Lee, K.; Jur, J. S.; Kim, D. H.; Parsons, G. N. Mechanisms for Hydrophilic/hydrophobic Wetting Transitions on Cellulose Cotton Fibers Coated using Al_2O_3 Atomic Layer Deposition. *J. Vac. Sci.Technol., A* **2012,** *30*, 01A163.
37. Kaialy, W; Alhalaweh, A; Velaga, S.P.; Nokhodchi, A. Influence of Lactose Carrier Particle Size on the Aerosol Performance of Budesonide from a Dry Powder Inaler. *Powder Technol.,* **2012**, *227*, 74-85.

38. Zellnitz, S; Roblegg, E; Pinto, J; Fröhlich, E. Delivery of Dry Powders to the Lungs: Influence of Particle Attributes from a Biological and Technological Point of View. *Curr. Drug Deliv*., **2019,** *16*, 180-194.

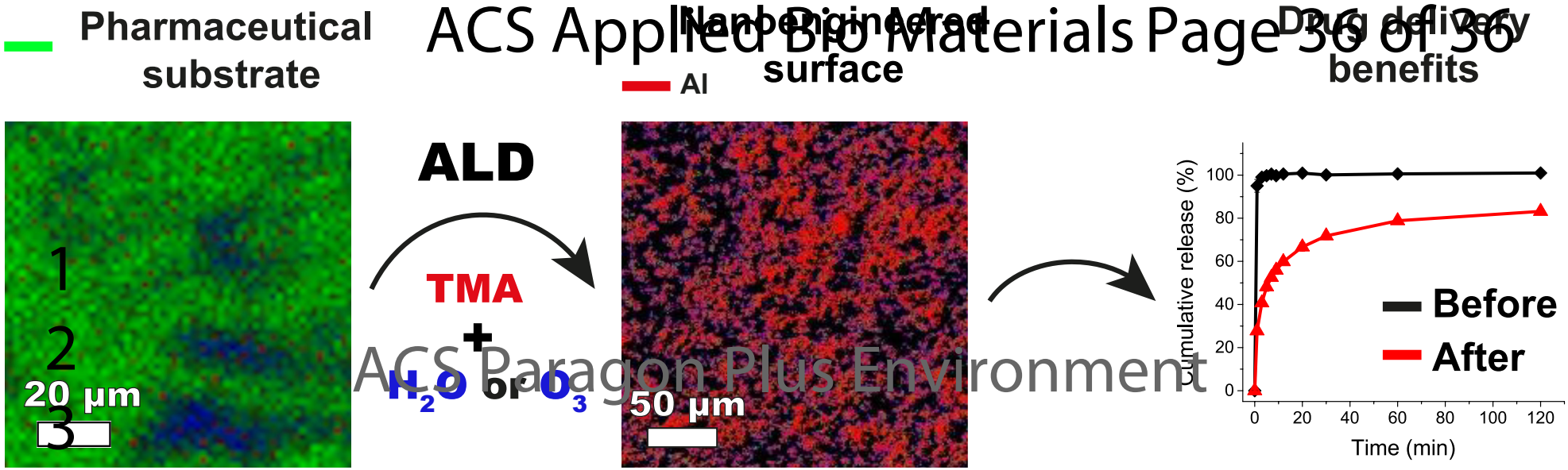

ACS Paragon Plus Environment